Author Contributions:

Conceptualization: R. Guardo, G. Ventura
Data curation: J. Prudencio
Formal analysis: R. Guardo
Funding acquisition: L. De Siena
Methodology: R. Guardo, J. Prudencio
Resources: L. De Siena
Software: R. Guardo, L. De Siena
Supervision: L. De Siena, G. Ventura
Validation: J. Prudencio, G. Ventura
Visualization: R. Guardo, L. De Siena
Writing – original draft: R. Guardo
Writing – review & editing: L. De Siena, J. Prudencio, G. Ventura

Imaging the Absorbing Feeding and Eruptive Pathways of Deception Island, Antarctica

R. Guardo[1,2,3] , **L. De Siena[2,4]** , **J. Prudencio[5]** , and **G. Ventura[6]**

[1]Instituto de Investigaciòn en Paleobiologìa y Geologìa (CONICET-UNRN), General Roca, Argentina, [2]TeMaS—Terrestrial Magmatic Systems Research Area, Johannes Gutenberg University, Mainz, Germany, [3]Sezione di Bologna, Istituto Nazionale di Geofisica e Vulcanologia, Bologna, Italy, [4]Institute of Geosciences, Johannes Gutenberg University, Mainz, Germany, [5]Departamento de Física Teórica y del Cosmos, Universidad de Granada, Granada, Spain, [6]Sezione di Roma, Istituto Nazionale di Geofisica e Vulcanologia, Roma, Italy

Abstract Deception Island is one of the most active and best-documented volcanoes in Antarctica. Since its last eruption in 1970, several geophysical surveys have targeted reconstructing its magmatic systems. However, geophysics fails to reconstruct the pathways magma and fluids follow from depth to erupt at the surface. Here, novel data selection strategies and multi-frequency absorption inversions have been framed in a Geographical Information System, using all available geological (vents and faults distribution), geochemical and geophysical knowledge of the volcano. The result is the detection of these eruptive pathways. The model offers the first image of the magma and associated fluids pathways feed the 1967, 1969, and 1970 eruptions. Results suggest that future ascending paths might lead to active research bases and zones of planned helicopter rescue. The connection between seismic absorption, temperature, and fluid content makes it a promising attribute for detecting and monitoring eruptions at active calderas.

Plain Language Summary Deception Island is the gateway for tourists to Antarctica and a laboratory to understand ice-capped volcanoes and their eruptions. While the Island has been the target of many geophysical studies, no clear tomographic model shows how deep eruptive pathways of its last eruptions have reached the surface in the 1960s and 1970s. This is a recurrent topic in volcano geophysics: dikes and fluid migrations develop across structures considered too small to be detected by tomographic techniques. This paper demonstrates that seismic absorption has sufficient sensitivity to temperature and fluid content to detect these pathways. Once integrated within a Geographical Information System with all the information we have on the volcano, the models resolve the feeding systems of these eruptions, from a tectonically deformed deep magma chamber to shallow cold dyke intrusions and fluid migrations still feeding the volcano today. The correlation between seismic absorption, temperature, and fluid content offers a new tool for detecting and monitoring shallow volcanic hazards.

1. Introduction

Deception Island originated less than 0.75 Ma ago (Smellie, 1988; Valencio et al., 1979), in the Plio-Pleistocene. It is located in the Bransfield Strait, between −62.893 and −63.021° south and between −60.751 and −60.495 west. This horseshoe-shaped caldera is located between the South Shetland Islands archipelago, at its north and the Antarctic Peninsula at its south (Figure 1, top right). It extends east-west and north-south for 12.85 and 14.41 km, respectively, thus covering an area of about 94.7 km² (Figure 1). The altitude of Deception Island varies from 160 m below sea level, in Port Foster, to its highest point, Mount Pond, at 539 m above sea level (Figure 1, bottom).

The interest in deciphering the magmatic system of Deception island has steadily grown due to the increasing numbers of tourists during the summer season and the presence of Argentinian and Spanish research bases. Studies conducted in this volcano have extensively covered: geochemistry (Álvarez-Valero et al., 2020; Aparicio et al., 1997; Geyer et al., 2019, 2021; Kusakabe et al., 2009; Somoza et al., 2004; Rey et al., 2002, and references therein), gravimetry, magnetic, and magnetotelluric (Catalán et al., 2014; Funaki et al., 2014; Pedrera et al., 2012; Smellie et al., 2002), satellite (Berrocoso et al., 2006, 2008) and seismology (Ben-Zvi et al., 2009; Luzón et al., 2011; Prudencio et al., 2013, 2015; Vila et al., 1995; Zandomeneghi et al., 2009).
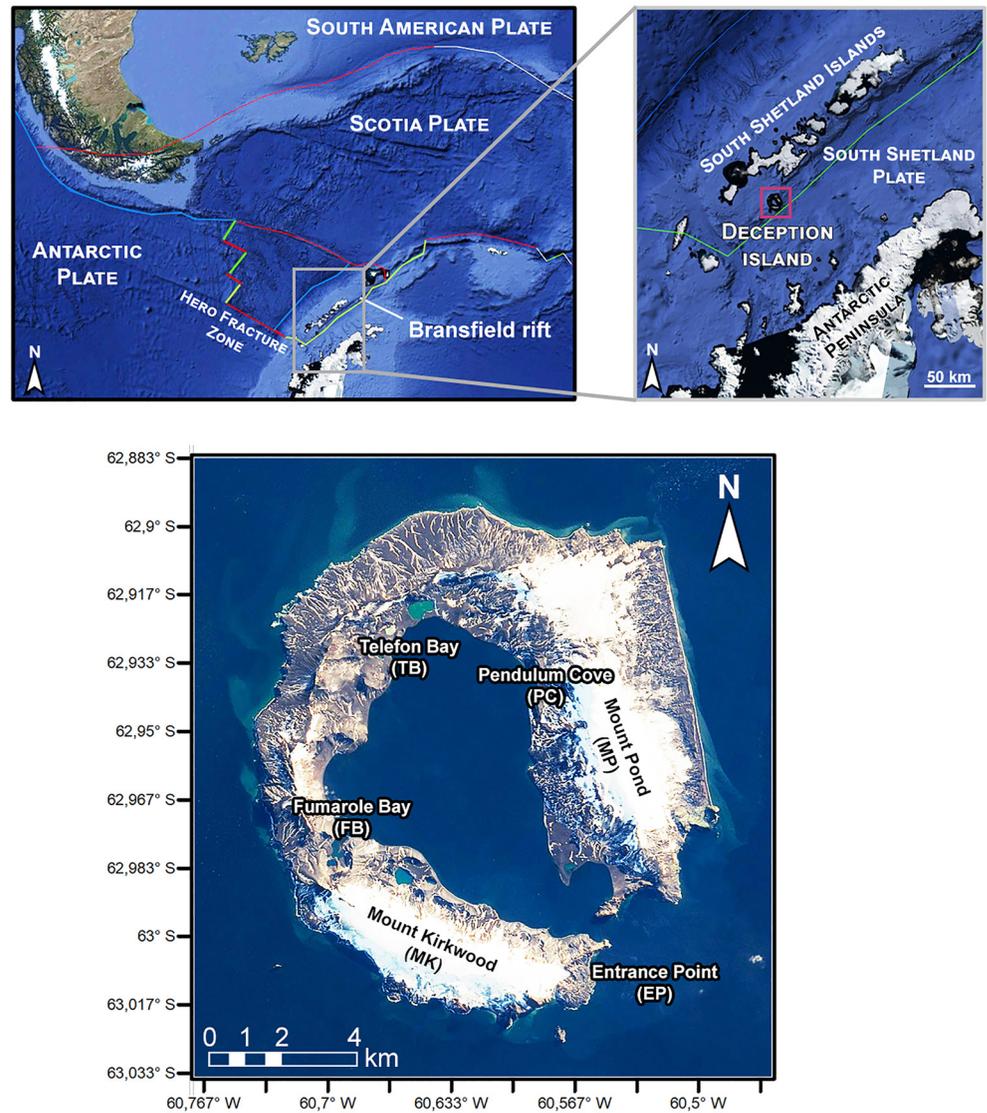
Figure 1. Simplified regional tectonic framework of the South Shetland Island (top). Deception Island satellite image with toponyms.

A particular focus has been on defining the deep volcanic structures through seismic tomographic studies (Vila et al., 1992, 1995). A massive improvement in the reconstruction of deep volcanic structures followed the TOMO-DEC experiment in 2005 (Ibáñez et al., 2017) and the velocity (Ben-Zvi et al., 2009; Zandomeneghi et al., 2009), attenuation, and scattering tomography (Del Pezzo et al., 2016; Prudencio et al., 2013, 2015) models obtained using its data. The detection potential of these techniques can be increased with novel tomography-driven selection strategies (Guardo & De Siena, 2022), particularly relevant when performing waveform-based techniques, as absorption tomography using multiple-scattering sensitivity kernels (Del Pezzo et al., 2016; Sketsiou et al., 2020). This technique has demonstrated enhanced detection potential on thermal anomalies, discriminating from hot fluid-filled network systems to the deformation effect of small-scale cold dike intrusions (∼0.3 km minimum spatial dimension) and caprock formations (De Siena et al., 2017).

Temperature, geochemistry, pore-pressure, and fluid content within fractures affect seismic absorption (Amoroso et al., 2017; De Landro et al., 2019; Di Martino et al., 2021; Tisato et al., 2015). This parameter is thus the ideal candidate to detect eruptive pathways for fluids and magma at volcanoes. We also lack an interpretation integrating all available geophysical imaging with the extensive interdisciplinary knowledge at Deception Island. By embedding absorption maps in a Geographical Information System (GIS) (Guardo & De Siena, 2017), we enable
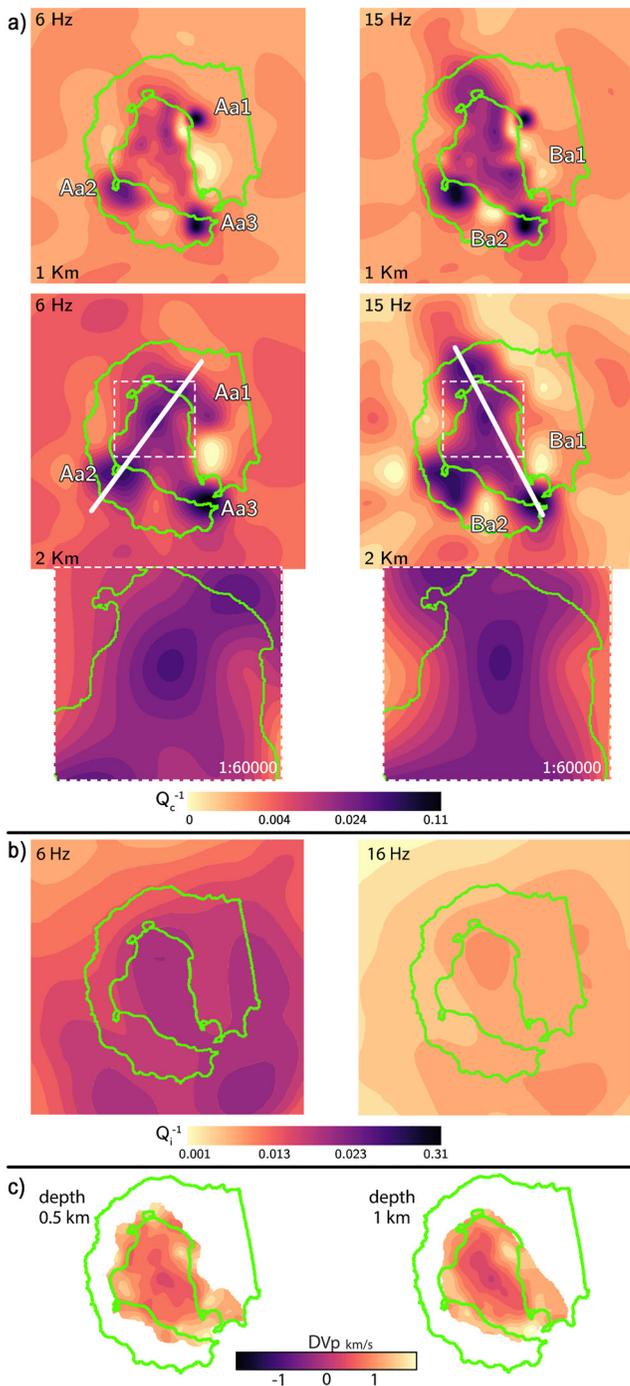
Figure 2. (a) Absorption maps at different frequencies and node spacings. High absorption: Aa1—Pendulum Cove area; Aa2—Fumarole Bay; Aa3—Entrance Point. Low absorption: Ba1—Mount Pond; Ba2—Mount Kirkwood. The continuous white lines show the primary absorption trends, while dashed lines contour and zoom on of their crossing point at 2 km node spacing. (b) The absorption maps of Prudencio et al. (2013) and (c) the velocity tomography of Zandomeneghi et al. (2009) are reproduced with the same color scale for comparison.

pattern recognition to benchmark the ability of geophysical imaging to detect eruptive pathways, supporting the interpretation of the processes that lead to eruptions. This knowledge, while extremely detailed when considering petrological data (Geyer et al., 2019), is at present difficult to connect with the broad structure of the feeding systems imaged with geophysics (Prudencio et al., 2015; Zandomeneghi et al., 2009). Recent eruptions generated by deep magma in the bay have happened at the border of the internal rim (Geyer et al., 2019; Smellie, 2002), as predicted by numerical and analog modeling (Mantiloni et al., 2021; Rivalta et al., 2019). However, the connections that bring magma and fluids to surface eruption remain undetected by geophysical imaging at this and other volcanoes (Schuler et al., 2015).

2. Data and Methods

We applied a multidisciplinary approach to a sub-data set of the TOMODEC seismic experiment conducted inside the bay and offshore Deception Island (Ibáñez et al., 2017; Prudencio et al., 2013). The method combines a detailed statistical analysis of the data designed for absorption tomography (Guardo & De Siena, 2022) with interpretations performed in a GIS environment. The original data set is described and made available by Ibáñez et al. (2017). The subset was used by Prudencio et al. (2013) to separate and map scattering attenuation from absorption using Gaussian sensitivity kernels. The selection process discriminated the best quality traces based on inversion-specific parameters (Guardo & De Siena, 2022). We describe differences for frequencies below (6 Hz, Figure 2) and above (15 Hz) the dominant frequency of the shots (12 Hz).

The method is a multi-frequency seismic tomography that uses 2D spatial coda-sensitivity kernels (Del Pezzo et al., 2016) to analyze the spatial distribution of coda quality factors (Q_c) (De Siena et al., 2017). The envelopes measured from data produced by the active shots are scattered diffusively. At a lapse time of 4 s after each shot absorption dominates over scattering, making Q_c^{-1} a direct marker of seismic absorption (Calvet & Margerin, 2013; Sketsiou et al., 2020). The analytical kernels are valid for the first 15 s from the origin-time of the shot (Del Pezzo et al., 2016) and used in the approximation that all the energy remains within the inversion grid at the lapse times considered (De Siena et al., 2017). This assumption is justified given: (a) the short transport mean free time of volcano-seismic signals produced by active surveys (Wegler, 2003); (b) the extension of the inversion grid (about 20 km^2) (De Siena et al., 2017). We perform a zero-order Tikhonov inversion where the damping value is a compromise between residuals and solution norm (Guardo & De Siena, 2022). The models have been tested in both frequency bands for resolution using chequerboard tests (Figures S1 and S2 in Supporting Information S1) and testing different damping parameters (Figures S3 and S4 in Supporting Information S1) for different node spacings.

We combine our maps with the available geological and geochemical information, specifically: with the distribution of vents (Geyer et al., 2019), the morphotectonic zonation of Deception Island (Paredes et al., 2006), the main tectonic features (Lopes et al., 2015), and the spatial distribution of arsenic (As) and manganese (Mn) (Somoza et al., 2004) (Figures 2–4). Our aim is to detect spatial correspondences among our images and these features. We select As and Mn distributions because the higher concentration of such elements give information on the location of submarine hydrothermal seeps and vents (Somoza et al., 2004). The multi-frequency maps were analyzed
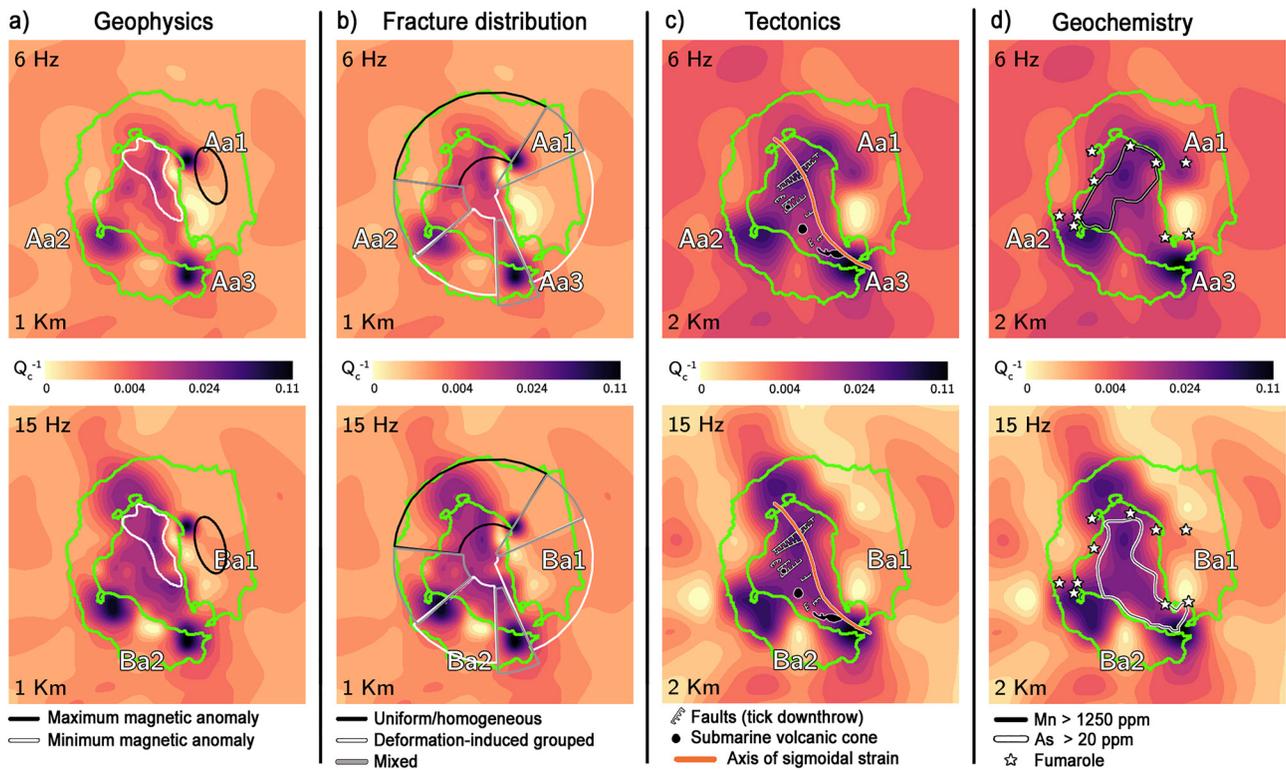
Figure 3. Comparison between the results and: (a) magnetic anomalies (Catalán et al., 2014); (b) morphotectonic zonation (Paredes et al., 2006); (c) main tectonic features obtained by Lopes et al. (2015) and sketched by Rey et al. (2002); (d) spatial distribution of arsenic (As) and manganese (Mn) (Somoza et al., 2004), where the lines contour the zones of highest concentration, and fumaroles (Rey et al., 2002).
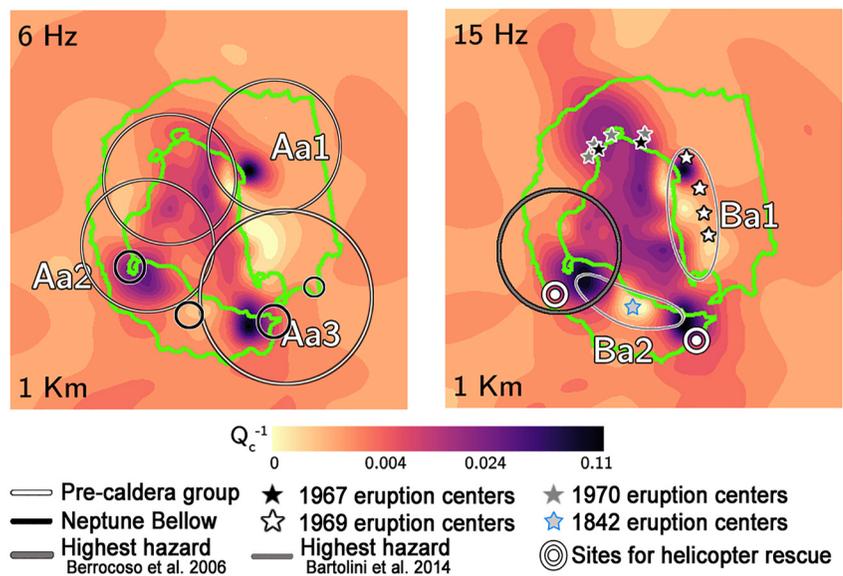
Figure 4. Comparison between the results at 1 km spacing and pre-caldera and Neptune Bellow eruptive centers identified by Hawkes (1961) (left). The stars show the eruptive centers of the last three eruptions derived from Baker et al. (1975), Pedrazzi et al. (2014), Pedrazzi et al. (2018) and Geyer et al. (2019). Gray lines contoured in black and white contour the zones of highest hazard identified by Berrocoso et al. (2006) and Bartolini et al. (2014), respectively.

within a GIS framework allowing the comparison in space with results from previous studies (Guardo & De Siena, 2017), with the assumption that higher frequencies image smaller features. High seismic absorption anomalies are interpreted as zones of magma emplacement or where geothermal fluids rise to the surface. In contrast, low seismic absorption anomalies mark zones impermeable to fluids or characterized by cooled magmatic residues.

3. Results

We resolve several high-absorption anomalies within the bay and across the rim (Figure 2a). At the same frequencies, the absorption maps have a resolution higher than those in Prudencio et al. (2013) (Figure 2b), showing stable, resolved features in the center of the island and across the caldera rim (Figures S1 and S2 in Supporting Information S1). At 6 Hz, we recognize a similar NNW-SSE high-absorption trend in the two absorption maps (Figures 2a and 2b), within the low-velocity anomaly identified by Zandomeneghi et al. (2009) (Figure 2c). The highest-absorption anomalies remained undetected in Prudencio et al. (2013), with these authors resolving a single high-absorption area at 16 Hz at the northern end of the NNW-SSE trend.

The high-absorption anomaly that covers the bay comprises NNW-SSE and NE-SW trends, visible especially at 2 km grid spacing (Figure 2a, white lines). The highest absorption anomaly within the bay is the crossing point between trends in the northern area of Port Foster (Figure 2a, dashed inset), also dominant in the maps of Prudencio et al. (2013) (Figure 2b). At 1 km node spacing, this anomaly appears elongated NNW-SSE, cross-cutting the eastern portion of the bay (Figure 2a). There are two low-absorption anomalies at both frequencies corresponding to ice-capped deformed regions comprised within Mount Pond (Ba1) and near Mount Kirkwood (Ba2). High absorption anomalies occur at the border of the caldera rim and are located at Pendulum Cove (Aa1), Fumarole Bay (Aa2), and Entrance Point (Aa3). Aa1 is near the Chilean station, destroyed during the eruption of 1969, while Aa2 is between the active Argentinean and Spanish research bases. The NNW-SSE high-absorption trend developing primarily through the bay also crosses the northern island. At 6 Hz, corresponding to larger heterogeneities and greater depths, its absorption maximum coincides with Telefon Bay and Lago Escondido, that is, the areas of the 1967 and 1970 eruptions.

4. Discussion

We discuss the relationship between the well-reconstructed portions of our models (Figure S1 in Supporting Information S1), the primary tectonic, hydrothermal, and volcanic structures, and inferred hot fluid/magma pathways within a GIS workspace. Based on the presented data and results, we focus on the shallower (less than 2 km depth) heat sources, lacking information on deeper structures.

4.1. Images of Tectonic-Controlled Magma and Fluid Sources

There is extensive geophysical evidence of the effect of the NNW-SSE-striking tectonics on the magmatic and hydrothermal activity on the island (Álvarez-Valero et al., 2020; Zandomeneghi et al., 2009). The wider absorption pattern largely corresponds to the area of uplift inside the basin (Cooper et al., 1998). It has the same orientation as the high-temperature anomaly within the bay, evidenced by Berrocoso et al. (2018). Submarine cones, craters and mounds aligned along a NNW-SSE axis have been highlighted since the early 1990s by seismic refraction studies (Martí et al., 1996; Rey et al., 1995). Most of the mounds are located within a radius of 3 km from the anomaly Aa2 or Aa3. The mounds close to the coastline, in front of Whalers Bay, are located at about 1 km of the Aa3 anomaly and are interpreted as the consequence of hydrothermal processes supporting the underwater volcanic structures. The Aa3 anomaly overlaps a possible, although uncertain, shallow intrusion or pyroclastic agglomerate overlayed by a submarine cone, as evidenced by seismic lines (Kowalewski et al., 1990; Martí et al., 1996). Besides the seismic refraction studies, geodetic anomalies show reactivation of the volcanic system following the seismic crises of the 90s Berrocoso et al. (2006) interpret this reactivation as caused by a magmatic intrusion at around 500 m b.s.l., located in the area of Fumarole Bay, coinciding with the Aa2 anomaly. Berrocoso et al. (2008) prove that NW-SE extensional and a NE-SW compressional patterns affected the island from 1991 to 2000 using the geodetic network. These patterns match the two high-absorption trends inside the bay (Figure 2a).

The NNW-SSE anomaly in the inner bay was detected in the past as a broad low-velocity (e.g., Figure 2c) and attenuation (Figure 2b, 6 Hz) feature encompassing the entire bay (Luzón et al., 2011; Prudencio et al., 2015; Vila et al., 1995; Zandomeneghi et al., 2009). Our study shows higher resolution on these structures, whose absorption signature is likely caused by hot hydrothermal fluids stored within the first 2 km of the crust (Geyer et al., 2019; Luzón et al., 2011). The spatial correlations support the inference that the highest-absorption anomaly in the northern bay represents the top of a high-temperature reservoir, appearing as the primary source for the recent eruptions of the volcano.

The NNW-SSE high-absorption trend coincides with a 2-km-conductor of similar orientation crossing the bay (Pedrera et al., 2012). These low-resistivity bodies are interpreted as a combination of partially molten material and hot fluids from the results of this and other potential-field surveys (Catalán et al., 2014; Funaki et al., 2014). The NNW-SSE-striking highest-absorption anomaly in the eastern part of the bay shows a strong spatial correlation with the minimum magnetic anomaly found by Catalán et al. (2014) and Funaki et al. (2014) (Figure 3a, while lines). The magnetic maxima are instead parallel to and located NE of the Ba1 low-absorption feature (Figure 3a, black oval) and interpreted by Catalán et al. (2014) and Funaki et al. (2014) as a cooled magmatic body. This interpretation and the ice cap covering the anomaly support the relation between low absorption and low-temperature bodies.

Faults and fractures have a proven high-absorption effect on seismic recordings if fluids permeate the systems, and generally drive wide absorption patterns (De Siena et al., 2017; Di Martino et al., 2021; Napolitano et al., 2020). The morpho-tectonic zoning projected on the cartographic traces carried out by Paredes et al. (2006) highlights the most superficial elements across the island. This study recognizes three zones (Figure 3b): the three high-absorption anomalies (Aa1-Aa3) fall within or are at the border of areas marked by the gray, mixed-deformation zone (Figure 3b), an expression of deep processes and high fumarole activity. Deep processes cause less deformation than the opening of fractures and vents at the surface, marked by the white zone. The correlation with the zones of mixed deformation shows how high absorption features express a deep connection path, primarily related to previous eruptions (see next section). The white zones mark instead the low-absorption expression of previous dike intrusions and fractures (Figure 3b, Ba1-Ba2).

Structural features appear to be the primary controller of the NE-SW and NNW-SSE high-absorption trends across the bay (De Rosa et al., 1995; Maestro et al., 2007) (Figure 2a). Lopes et al. (2015) generated a tectonic map highlighting a Riedel deformation model. At 1 km node spacing, the widest high-absorption anomaly within the bay has an orientation between NS and NNW-SSE, coinciding with the Hero Fracture Zone, almost orthogonal to the extensive dynamics of the Strait of Bransfield. The NE-SW anomaly coincides with submarine faults of similar strike, whose downthrow focuses on the central part of the anomaly (Figure 3c). The anomalies at 2-km node spacing show a sigmoidal shape at both frequencies, but particularly at 15 Hz, stretching in a direction roughly parallel to the regional distension (Figure 3c, orange line). This sigmoidal shape is interpreted as the signature of how the caldera subsided (Lopes et al., 2015). At 6 Hz (thus at greater depths (∼1 km)) the NNE-SSW high-absorption axis is parallel to Riedel's R fractures in the system proposed by Lopes et al. (2015). The spatial correlation between high absorption and tectonic features thus suggests that the high-absorption anomalies detect the shallower product of deeper tectonically-controlled reservoirs within the bay.

The preferential NW-SE and NNE-SSW high-absorption orientations also coincide with the spatial variations of specific hydrothermal outputs, whose location is controlled by tectonics (Álvarez-Valero et al., 2020; De Rosa et al., 1995) (Figure 3d). There is extensive evidence of the dependence of seismic attenuation and absorption on thermal variations at the mantle, crustal, and volcano scales (Abers et al., 2006; Cammarano & Romanowicz, 2008; De Lorenzo et al., 2001), with high thermal potential the most likely explanation for absorption increases at locations Aa1-Aa3. On the other hand, geochemical variations caused by different fluid compositions and saturation levels can equally change attenuation in space (Amoroso et al., 2017; De Landro et al., 2019), especially within an active hydrothermal system (Di Martino et al., 2021). The NE-SW and NNE-SSW high-absorption trends correspond to the measured variations in Mn and As, respectively (Rey et al., 2002; Somoza et al., 2004) (Figure 3d). At 15 Hz (shallower depths) the orientation of the high-absorption anomaly coincides with the axis of maximum concentration of Mn. This signature is related to the interaction between the sediments and fluids emitted from the submarine volcanic vents, which also develop NE-SW (Martí et al., 1996; Somoza et al., 2004). At 6 Hz, the NNW-SSE high-absorption signature aligns to the maximum distribution of As (Figure 3d). High As values are associated with water-rock interactions more than magma (Somoza et al., 2004), providing further evidence that

magma storage is likely deeper than our investigation volume, and absorption anomalies are primarily controlled by tectonics.

Fumarolic centers are the most superficial expression of a deeper hydrothermal system. Gaseous components such as helium and carbon dioxide in fumaroles come from the underlying magma and are released to the surface through faults, and fractures (Kusakabe et al., 2009). The fumaroles distribute consistently in regions of high absorption (Rey et al., 2002) (Figure 3d, stars). Similar correlations between attenuation contrasts and sub-vertical rise of fluids have been demonstrated comparing attenuation models and spring locations across the Pollino fault network (Sketsiou et al., 2021). Absorption is a direct marker of fluids with high-concentration of gas, which is a proven trigger of high attenuation at the laboratory (Tisato et al., 2015) and volcanic scales (De Siena et al., 2017). The source of these fluids is the complex network of individual shallow magma storage zones with variable volumes, compositions and sizes, and placed at depths approximately between 10 and 2 km b.s.l. (Geyer et al., 2019). The detected high-absorption anomalies represent areas where fluids at high temperatures uprise, migrating preferentially through faults and fractures located at the border of the primary high-absorption volumes (hot-fluids reservoirs).

4.2. Geophysical Image of Eruptive Paths Controlling Fluid Migrations

The highest-absorption anomalies correspond to ancient eruptive cones and areas currently affected by volcanic emissions (Smellie et al., 2002). Hawkes (1961) provide maps and sketches of geological formations focusing on the areas that erupted before 1967, like the volcanism of the pre-caldera group, that is, the Port Foster Group, within which the volcanism of Telefon Bay is placed (Figure 4, large white circles). The Aa1-Aa3 anomalies and the crossing point between NE-SW and NNW-SSE high-absorption trends leading to the site of the 1967/1970 eruption (Telefon Bay - see the zoom in Figure 2a) are all less than 2 km distant from the proposed center of these ancient eruptions. Hawkes (1961) also describes the second volcanic event of the island and its eruptive centers (falling within the Neptune Bellow Group and following the Port Foster Group); these centers coincide with the Mount Pond Group in the Stonethrow Ridge Formation (Smellie, 2001). Among the four highlighted centers (Figure 4, black circles), Vapor Col and Entrance Point coincide with the Aa2 and Aa3 anomalies. In addition, the Ba2 anomaly is located near Mount Kirkwood, where the authors place two additional volcanic cones hidden under the ice cap. The cone located in the South East Point zone could not be linked to absorption features, but this zone remains unresolved in our models (Figure S1 in Supporting Information S1).

The high-absorption anomalies are often co-located with the centers of the 1967, 1969 and 1970 eruptions (Figure 4, stars). In particular, the area related to the 1967 and 1970 eruptions coincides with the northern termination of the anomaly oriented NNW-SSE, while the northern vent of the 1969 eruptive fissure corresponds to Aa1 in the Pendulum Cove area. These geographical correspondences show high-absorption anomalies that can represent: (a) the magmatic residues of past eruptions; (b) newly-formed shallow magma storage zones; (c) or, more likely, high-temperature fluids rising through the pathways formed during the previous eruptions. The NNW-SSE elongated low-attenuation strip Ba1 located south of the high attenuation zone Aa1 follows the trace of a cooled dike responsible for the 1969 eruption, opening several vents across its path. We infer that Aa1, which is located at the northern tip of the eruptive fractures where the eruption originated, represents the shallowest feature of the volcanic conduit, still hot today. The high-absorption areas in our maps generally correspond to areas of higher thermal potential (Paredes et al., 2006). Low-absorption anomalies appear instead as the seismological signature of cooled erupted material due to the local cold weather conditions. Similar processes could affect materials under the ice-capped Mt. Kirkwood, corresponding to the second low-absorption anomaly (Ba2), which corresponds to the 1842 eruption vents at Mt. Kirkwood (De Rosa et al., 1995).

The ability of coda waves to detect shallow, unconsolidated, and cooled systems has been proven when targeting debris avalanches, like the one at Mount St. Helens volcano in 1980 (De Siena et al., 2016; Gabrielli et al., 2020), and shallow dike intrusions (De Siena et al., 2017). The assessment of the Ba1 and Ba2 anomalies as rapidly-cooled erupted materials (Figure 4, white-contoured gray lines, right) is supported by their spatial correspondence with historical vents. The vent distribution allowed Bartolini et al. (2014) to define the spatial arrangement of the highest susceptibility values (probability of vent opening) in the hazard map of Deception Island. The hotter zones coincide with the high-absorption anomaly Aa2 in the Fumarole Bay area (Figure 4, black-contoured gray circle) where the hydrothermal emissions and sub-surface hot zones occur. This implies that the hazard maps or, more in general, hazard evaluations should include the results of attenuation studies in addition to volcanological,

geochemical, and other geophysical data (Berrocoso et al., 2006). At Deception, hazard maps are essential to establish escape routes for scientists and tourists in the case of an impending eruption. The connection we infer between temperature and seismic absorption could be a central ingredient for a better hazard assessment of the island. In particular, we focus attention on Aa2 and the Aa3 anomaly located at the island entrance. Both anomalies coincide with areas suggested for landing and takeoff of rescue helicopters (Smellie et al., 2002). Our analysis identifies these anomalies as potential reservoirs from which hazardous materials could rise to the surface.

5. Conclusions

Due to its high sensitivity to thermal anomalies, absorption imaging detects recent (hot) and older (cold) magma feeding systems and paths for fluids at Deception Island. Two over three resolved high-absorption anomalies coincide with areas where magma ascended in the past, feeding hot gas-bearing fluids to fumarolic fields after seismic crises. Several eruptive centers appear connected to the persistent high-absorption NNW-SSE trending anomaly cross-cutting the bay and parallel to the current extension of the Bransfield Strait. The point of highest absorption in the NE bay connects with two smaller high-absorption anomalies located near Pendulum Cove and Fumarole Bay. One of these anomalies matches the eruptive center of the 1969 eruption. There is instead consistent evidence that low-absorption zones mark the most hazardous, shallow paths followed by floods and fissures within ice from the first eruptive centers.

Our results represent the most detailed seismic image of the shallower feeding system of Deception Island and demonstrate that absorption tomography provides direct images of the regions with higher thermal gradients and increased gas concentration in fluids. This apparent link makes seismic absorption a high-resolution tool for imaging and monitoring how magma and fluids upraise or are stored at very shallow depths. We focus on the potential hazard associated with the high-absorption anomalies near the active research bases and, especially, Entrance Point. This area shows no recent volcanic activity or hydrothermal output and coincides with established escape routes during volcanic unrest.

Data Availability Statement

The data sets used for the Qc analysis are those obtained from the Qc data cleaning process (Guardo & De Siena, 2022) and they are stored at: https://doi.org/10.5281/zenodo.6561124. The final absorption model is obtained using a fork of the MuRAT2D code, whose final release is available at: https://zenodo.org/badge/latest-doi/493744216. Additionally, at the same link it is possible to download the ArcPy codes for the import and map creation.

References

Abers, G. A., van Keken, P. E., Kneller, E. A., Ferris, A., & Stachnik, J. C. (2006). The thermal structure of subduction zones constrained by seismic imaging: Implications for slab dehydration and wedge flow. *Earth and Planetary Science Letters*, *241*(3–4), 387–397. https://doi.org/10.1016/j.epsl.2005.11.055

Álvarez-Valero, A., Gisbert, G., Aulinas, M., Geyer, A., Kereszturi, G., Polo-Sánchez, A., et al. (2020). δD and δ18O variations of the magmatic system beneath Deception Island volcano (Antarctica): Implications for magma ascent and eruption forecasting. *Chemical Geology*, *542*, 119595. https://doi.org/10.1016/j.chemgeo.2020.119595

Amoroso, O., Russo, G., De Landro, G., Zollo, A., Garambois, S., Mazzoli, S., et al. (2017). From velocity and attenuation tomography to rock physical modeling: Inferences on fluid-driven earthquake processes at the Irpinia fault system in southern Italy. *Geophysical Research Letters*, *44*(13), 6752–6760. https://doi.org/10.1002/2016gl072346

Aparicio, A., Risso, C., Viramonte, J., Menegatti, M., & Petrinovic, I. (1997). El volcanismo de isla decepcion (Peninsula Antartica). *Boletin Geologico y Minero*, *108*(3), 19–42.

Baker, P., McReath, I., Harvey, M., Roobol, M., & Davies, T. (1975). *The geology of the South Shetland Islands: V. Volcanic evolution of Deception Island* (Vol. 78). British Antarctic Survey.

Bartolini, S., Geyer, A., Martí, J., Pedrazzi, D., & Aguirre-Díaz, G. (2014). Volcanic hazard on Deception Island (South Shetland Islands, Antarctica). *Journal of Volcanology and Geothermal Research*, *285*, 150–168. https://doi.org/10.1016/j.jvolgeores.2014.08.009

Ben-Zvi, T., Wilcock, W. S., Barclay, A. H., Zandomeneghi, D., Ibáñez, J. M., & Almendros, J. (2009). The P-wave velocity structure of Deception Island, Antarctica, from two-dimensional seismic tomography. *Journal of Volcanology and Geothermal Research*, *180*(1), 67–80. https://doi.org/10.1016/j.jvolgeores.2008.11.020

Berrocoso, M., Fernández-Ros, A., Ramírez, M., Salamanca, J., Torrecillas, C., Pérez-Peña, A., et al. (2008). Geodetic research on Deception Island and its environment (South Shetland Islands, Bransfield sea and Antarctic Peninsula) during Spanish Antarctic campaigns (1987–2007). In *Geodetic and geophysical observations in Antarctica* (pp. 97–124). Springer.

Berrocoso, M., García-García, A., Martín-Dávila, J., Catalán-Morollón, M., Astiz, M., Ramírez, M. E., et al. (2006). Geodynamical studies on Deception Island: DECVOL and GEODEC Projects. In *Antarctica* (pp. 283–287). Springer.

Berrocoso, M., Prates, G., Fernández-Ros, A., Peci, L., de Gil, A., Rosado, B., et al. (2018). Caldera unrest detected with seawater temperature anomalies at Deception Island, Antarctic Peninsula. *Bulletin of Volcanology*, *80*(4), 41. https://doi.org/10.1007/s00445-018-1216-2

Calvet, M., & Margerin, L. (2013). Lapse-time dependence of coda Q: Anisotropic multiple-scattering models and application to the Pyrenees. *Bulletin of the Seismological Society of America*, *103*(3), 1993–2010. https://doi.org/10.1785/0120120239

Cammarano, F., & Romanowicz, B. (2008). Radial profiles of seismic attenuation in the upper mantle based on physical models. *Geophysical Journal International*, *175*(1), 116–134. https://doi.org/10.1111/j.1365-246x.2008.03863.x

Catalán, M., Martos, Y. M., Galindo-Zaldívar, J., & Funaki, M. (2014). Monitoring the evolution of Deception Island volcano from magnetic anomaly data (South Shetland Islands, Antarctica). *Global and Planetary Change*, *123*, 199–212. https://doi.org/10.1016/j.gloplacha.2014.07.018

Cooper, A., Smellie, J., & Maylin, J. (1998). Evidence for shallowing and uplift from bathymetric records of Deception Island, Antarctica. *Antarctic Science*, *10*(4), 455–461. https://doi.org/10.1017/s0954102098000558

De Landro, G., Serlenga, V., Amoroso, O., Russo, G., Festa, G., & Zollo, A. (2019). High resolution attenuation images from active seismic data: The case study of Solfatara volcano (southern Italy). *Frontiers of Earth Science*, *295*.

De Lorenzo, S., Gasparini, P., Mongelli, F., & Zollo, A. (2001). Thermal state of the Campi Flegrei caldera inferred from seismic attenuation tomography. *Journal of Geodynamics*, *32*(4–5), 467–486. https://doi.org/10.1016/s0264-3707(01)00044-8

Del Pezzo, E., Ibanez, J., Prudencio, J., Bianco, F., & De Siena, L. (2016). Absorption and scattering 2-D volcano images from numerically calculated space-weighting functions. *Geophysical Journal International*, *206*(2), 742–756. https://doi.org/10.1093/gji/ggw171

De Rosa, R., Mazzuoli, R., Omarini, R., Ventura, G., & Viramonte, J. (1995). A volcanological model for the historical eruptions at Deception Island (Bransfield Strait, Antarctica).

De Siena, L., Amoruso, A., Pezzo, E. D., Wakeford, Z., Castellano, M., & Crescentini, L. (2017). Space-weighted seismic attenuation mapping of the aseismic source of Campi Flegrei 1983–1984 unrest. *Geophysical Research Letters*, *44*(4), 1740–1748. https://doi.org/10.1002/2017GL072507

De Siena, L., Calvet, M., Watson, K. J., Jonkers, A., & Thomas, C. (2016). Seismic scattering and absorption mapping of debris flows, feeding paths, and tectonic units at Mount St. Helens volcano. *Earth and Planetary Science Letters*, *442*, 21–31. https://doi.org/10.1016/j.epsl.2016.02.026

Di Martino, M. D. P., De Siena, L., Healy, D., & Vialle, S. (2021). Petro-mineralogical controls on coda attenuation in volcanic rock samples. *Geophysical Journal International*, *226*(3), 1858–1872. https://doi.org/10.1093/gji/ggab198

Funaki, M., Higashino, S.-I., Sakanaka, S., Iwata, N., Nakamura, N., Hirasawa, N., et al. (2014). Small unmanned aerial vehicles for aeromagnetic surveys and their flights in the South Shetland Islands, Antarctica. *Polar Science*, *8*(4), 342–356. https://doi.org/10.1016/j.polar.2014.07.001

Gabrielli, S., De Siena, L., Napolitano, F., & Del Pezzo, E. (2020). Understanding seismic path biases and magmatic activity at Mount St Helens volcano before its 2004 eruption. *Geophysical Journal International*, *222*(1), 169–188. https://doi.org/10.1093/gji/ggaa154

Geyer, A., Álvarez-Valero, A. M., Gisbert, G., Aulinas, M., Hernández-Barreña, D., Lobo, A., & Martí, J. (2019). Deciphering the evolution of Deception Island's magmatic system. *Scientific Reports*, *9*(1), 1–14. https://doi.org/10.1038/s41598-018-36188-4

Geyer, A., Pedrazzi, D., Almendros, J., Berrocoso, M., López-Martínez, J., Maestro, A., et al. (2021). Deception island in volcanism in Antarctica: 200 million years of subduction, rifting and continental break-up. *Geological Society of London Memoirs*. https://doi.org/10.1144/M55-2018-56

Guardo, R., & De Siena, L. (2017). Integrating ambient noise with GIS for a new perspective on volcano imaging and monitoring: The case study of Mt. Etna. *Journal of Volcanology and Geothermal Research*, *347*, 397–407. https://doi.org/10.1016/j.jvolgeores.2017.10.007

Guardo, R., & De Siena, L. (2022). Semi-automated inversion-specific data selection for volcano tomography. *Frontiers of Earth Science*, *473*. https://doi.org/10.3389/feart.2022.849152

Hawkes, D. (1961). *The geology of the South Shetland Islands: II. The geology and petrology of Deception Island* (Vol. 27). HMSO.

Ibáñez, J. M., Díaz-Moreno, A., Prudencio, J., Zandomeneghi, D., Wilcock, W., Barclay, A., et al. (2017). Database of multi-parametric geophysical data from the TOMO-DEC experiment on Deception Island, Antarctica. *Scientific Data*, *4*(1), 170128. https://doi.org/10.1038/sdata.2017.128

Kowalewski, W., Rudowski, S., & Zalewski, S. M. (1990). Seismoacoustic studies within flooded part of the caldera of the Deception Island, West Antarctica. *Polish Polar Research*, 259–266.

Kusakabe, M., Nagao, K., Ohba, T., Seo, J. H., Park, S.-H., Lee, J. I., & Park, B.-K. (2009). Noble gas and stable isotope geochemistry of thermal fluids from Deception Island, Antarctica. *Antarctic Science*, *21*(3), 255–267. https://doi.org/10.1017/s0954102009001783

Lopes, F. C., Caselli, A., Machado, A., & Barata, M. (2015). The development of the Deception Island volcano caldera under control of the Bransfield Basin sinistral strike-slip tectonic regime (NW Antarctica). *Geological Society, London, Special Publications*, *401*(1), 173–184. https://doi.org/10.1144/sp401.6

Luzón, F., Almendros, J., & García-Jerez, A. (2011). Shallow structure of Deception Island, Antarctica, from correlations of ambient seismic noise on a set of dense seismic arrays. *Geophysical Journal International*, *185*(2), 737–748. https://doi.org/10.1111/j.1365-246x.2011.04962.x

Maestro, A., Somoza, L., Rey, J., Martínez-Frías, J., & López-Martínez, J. (2007). Active tectonics, fault patterns, and stress field of Deception Island: A response to oblique convergence between the Pacific and Antarctic plates. *Journal of South American Earth Sciences*, *23*(2–3), 256–268. https://doi.org/10.1016/j.jsames.2006.09.023

Mantiloni, L., Davis, T. G., Rojas, A. B., & Rivalta, E. (2021). Stress inversion in a gelatin box: Testing eruptive vent location forecasts with analog models. *Geophysical Research Letters*, *48*(6), GL090407. https://doi.org/10.1029/2020GL090407

Martí, J., Vila, J., & Rey, J. (1996). Deception Island (Bransfield Strait, Antarctica): An example of a volcanic caldera developed by extensional tectonics. *Geological Society, London, Special Publications*, *110*(1), 253–265. https://doi.org/10.1144/gsl.sp.1996.110.01.20

Napolitano, F., De Siena, L., Gervasi, A., Guerra, I., Scarpa, R., & La Rocca, M. (2020). Scattering and absorption imaging of a highly fractured fluid-filled seismogenetic volume in a region of slow deformation. *Geoscience Frontiers*, *11*(3), 989–998. https://doi.org/10.1016/j.gsf.2019.09.014

Paredes, C., Pérez-López, R., Giner-Robles, J., de la Vega, R., García-García, A., & Gumiel, P. (2006). Spatial distribution of morpholineaments and tectonic zoning in the Deception Island (South Shetland, Antarctica). *Geogaceta*, *37*, 75–78.

Pedrazzi, D., Aguirre-Díaz, G., Bartolini, S., Martí, J., & Geyer, A. (2014). The 1970 eruption on Deception Island (Antarctica): Eruptive dynamics and implications for volcanic hazards. *Journal of the Geological Society*, *171*(6), 765–778. https://doi.org/10.1144/jgs2014-015

Pedrazzi, D., Németh, K., Geyer, A., Álvarez-Valero, A. M., Aguirre-Díaz, G., & Bartolini, S. (2018). Historic hydrovolcanism at Deception Island (Antarctica): Implications for eruption hazards. *Bulletin of Volcanology*, *80*(1), 11. https://doi.org/10.1007/s00445-017-1186-9

Pedrera, A., Ruiz-Constán, A., Heredia, N., Galindo-Zaldívar, J., Bohoyo, F., Marín-Lechado, C., et al. (2012). The fracture system and the melt emplacement beneath the Deception Island active volcano, South Shetland Islands, Antarctica. *Antarctic Science*, *24*(2), 173–182. https://doi.org/10.1017/s0954102011000794

Prudencio, J., De Siena, L., Ibáñez, J., Del Pezzo, E., Garcia-Yeguas, A., & Diaz-Moreno, A. (2015). The 3D attenuation structure of Deception Island (Antarctica). *Surveys in Geophysics*, *36*(3), 371–390. https://doi.org/10.1007/s10712-015-9322-6

Prudencio, J., Ibáñez, J. M., García-Yeguas, A., Del Pezzo, E., & Posadas, A. M. (2013). Spatial distribution of intrinsic and scattering seismic attenuation in active volcanic islands–II: Deception Island images. *Geophysical Journal International*, *195*(3), 1957–1969. https://doi.org/10.1093/gji/ggt360

Rey, J., Maestro, A., Somoza, L., & Smellie, J. (2002). Submarine morphology and seismic stratigraphy of Port Foster. In J. López-Martínez, J. L. Smellie, J. W. Thomson, & M. Thomson (Eds.), *Geology and geomorphology of deception island* (pp. 40–46). British Antarctic Survey.

Rey, J., Somoza, L., & Martínez-Frías, J. (1995). Tectonic, volcanic, and hydrothermal event sequence on Deception Island (Antarctica). *Geo-Marine Letters*, *15*(1), 1–8. https://doi.org/10.1007/bf01204491

Rivalta, E., Corbi, F., Passarelli, L., Acocella, V., Davis, T., & Vito, M. A. (2019). Stress inversions to forecast magma pathways and eruptive vent location. *Science Advances*, *5*(7), eaau9784. https://doi.org/10.1126/sciadv.aau9784

Schuler, J., Greenfield, T., White, R. S., Roecker, S. W., Brandsdóttir, B., Stock, J. M., et al. (2015). Seismic imaging of the shallow crust beneath the Krafla central volcano, NE Iceland. *Journal of Geophysical Research: Solid Earth*, *120*(10), 7156–7173. https://doi.org/10.1002/2015jb012350

Sketsiou, P., De Siena, L., Gabrielli, S., & Napolitano, F. (2021). 3-D attenuation image of fluid storage and tectonic interactions across the Pollino fault network. *Geophysical Journal International*, *226*(1), 536–547. https://doi.org/10.1093/gji/ggab109

Sketsiou, P., Napolitano, F., Zenonos, A., & De Siena, L. (2020). New insights into seismic absorption imaging. *Physics of the Earth and Planetary Interiors*, *298*, 106337. https://doi.org/10.1016/j.pepi.2019.106337

Smellie, J. (1988). Recent observations on the volcanic history of Deception Island, South Shetland Islands (No. 81). In *British antarct surv high cross madingley rd, Cambridge, England cb3 0et*.

Smellie, J. (2001). Lithostratigraphy and volcanic evolution of deception island, South Shetland Islands. *Antarctic Science*, *13*(2), 188–209. https://doi.org/10.1017/s0954102001000281

Smellie, J. (2002). The 1969 subglacial eruption on Deception Island (Antarctica): Events and processes during an eruption beneath a thin glacier and implications for volcanic hazards. *Geological Society, London, Special Publications*, *202*(1), 59–79. https://doi.org/10.1144/gsl.sp.2002.202.01.04

Smellie, J., López-Martínez, J., Headland, R., Hernández-Cifuentes, F., Maestro, A., Millar, I., et al. (2002). *Geology and geomorphology of Deception Island*. British Antarctic Survey.

Somoza, L., Martınez-Frıas, J., Smellie, J., Rey, J., & Maestro, A. (2004). Evidence for hydrothermal venting and sediment volcanism discharged after recent short-lived volcanic eruptions at Deception Island, Bransfield Strait, Antarctica. *Marine Geology*, *203*(1–2), 119–140. https://doi.org/10.1016/s0025-3227(03)00285-8

Tisato, N., Quintal, B., Chapman, S., Podladchikov, Y., & Burg, J.-P. (2015). Bubbles attenuate elastic waves at seismic frequencies: First experimental evidence. *Geophysical Research Letters*, *42*(10), 3880–3887. https://doi.org/10.1002/2015gl063538

Valencio, D. A., Mendía, J., & Vilas, J. F. (1979). Palaeomagnetism and K sbnd Ar age of Mesozoic and Cenozoic igneous rocks from Antarctica. *Earth and Planetary Science Letters*, *45*(1), 61–68. https://doi.org/10.1016/0012-821x(79)90107-9

Vila, J., Correig, A. M., & Martí, J. (1995). Attenuation and source parameters at Deception Island (South Shetland Islands, Antarctica). *Pure and Applied Geophysics*, *144*(2), 229–250. https://doi.org/10.1007/bf00878633

Vila, J., Marti, J., Ortiz, R., Garcia, A., & Correig, A. M. (1992). Volcanic tremors at Deception Island (South Shetland Islands, Antarctica). *Journal of Volcanology and Geothermal Research*, *53*(1–4), 89–102. https://doi.org/10.1016/0377-0273(92)90076-p

Wegler, U. (2003). Analysis of multiple scattering at Vesuvius volcano, Italy, using data of the TomoVes active seismic experiment. *Journal of Volcanology and Geothermal Research*, *128*(1–3), 45–63. https://doi.org/10.1016/s0377-0273(03)00246-4

Zandomeneghi, D., Barclay, A., Almendros, J., Ibañez Godoy, J. M., Wilcock, W. S., & Ben-Zvi, T. (2009). Crustal structure of Deception Island volcano from P wave seismic tomography: Tectonic and volcanic implications. *Journal of Geophysical Research*, *114*(B6), B06310. https://doi.org/10.1029/2008jb006119